Molecular Dynamics Simulation of Electrical Resistivity in Sintering Process of Nanoparticle Silver Inks

Yi Zhang[1], Linmin Wu[1], Xingye Guo[1], Yeon-Gil Jung[2], Jing Zhang[1]*

1. Department of Mechanical Engineering, Indiana University-Purdue University Indianapolis, Indianapolis, IN 46202, USA

2. School of Materials Science and Engineering, Changwon National University, 20, Changwondaehak-ro, 641-773, Changwon, Gyeongnam, Republic of Korea

*Email: jz29@iupui.edu; Phone: 317-278-7186; Fax:317-274-9744

Abstract

A molecular dynamics (MD) model is developed to simulate low temperature sintering of silver nanoparticles and resultant resistivity. Due to the high surface to volume ratio, nanoparticle silver inks can sinter at low thermal curing temperatures, which are used in intense pulsed light (IPL) sintering process. In this study, the configurational change of nanoparticle silver during sintering is studied using the MD model. Then the resultant electric resistivity is calculated using the Reimann-Weber formula. The simulation results show that the resistivity decreases rapidly in the initial sintering stage, due to the fast neck formation and growth. Additionally, the predicted temperature-dependent resistivity evolutions are in good agreement with both experimental measurements and analytical sintering model, indicating that the resistivity decreases with increasing sintering temperature. The model provides a design tool for optimizing IPL process.

KEYWORDS: metals; nanostructures; diffusion; electrical properties

---

This is the author's manuscript of the article published in final edited form as:
Zhang, Y., Wu, L., Guo, X., Jung, Y.-G., & Zhang, J. (2016). Molecular dynamics simulation of electrical resistivity in sintering process of nanoparticle silver inks. Computational Materials Science, 125, 105–109.
https://doi.org/10.1016/j.commatsci.2016.08.047

1. Introduction

Recently, sintering of nano-inks has attracted interests for developing flexible electronic devices [1]. Selective laser and intense pulsed light (IPL) become particularly attractive due to their low processing temperatures [2, 3]. Nanoparticles, owing to their high surface to volume ratio, are suitable for nano-inks which can be sintered at low temperatures even at 10% of their melting points [4]. One of key criteria determining the performance of a printed electronics is the electrical conductivity, which is mainly affected by sintering behavior of nanoparticles [5]. In a typical IPL sintering process, metal nano-particles are sintered by intense pulse at room temperature. Nano-inks with metal particles (~5 nm, usually copper or silver) are firstly dried to form a solid thin film. The film is placed on the top of a polymer substrate (glass fiber, polyimide, polyethylene or polypropylene) and then subject to a xenon flash lamp exposure. When the lamp is triggered, a high electrical current (1000 A) is released by a charged supercapacitor (4000 μF) in the time range of 1-10 ms. During this process, an optical spectrum of light with wavelength from 160 nm to 2.5 mm is emitted to sinter the metal particles. Therefore, a complex shaped conductive network is fabricated [2].

The electrical resistivity of silver nanoparticles thermally cured at low temperatures has been studied from experimental measurements [6, 7]. The results show that the sintering time for nano-inks may have a considerably effect on electrical conductivity. For this reason, it is imperative to understand the sintering process of silver nanoparticles and its influence on the performance. However, for nano-inks printing process, it is often much more complicated. Process like IPL or moving laser source often leads to non-uniform microstructures with a short sintering time. In parallel to experiments, two-particle micromechanical model was developed with geometric assumption at particle contact to predict diffusion [8]. However, these models may not

be applicable to nano-inks sintering, due to nano-sized particles and the complexity in IPL process [9]. Additionally, finite element model [10], Monte Carlo simulation [11], and molecular dynamics simulations were developed to understand the sintering process [12-14]. Moitra *et al.* [14] studied the material transport mechanisms of powder bed sintering by molecular dynamics simulation. The diffusion mechanisms and activation energy for various types of mass transport were computed by using geometric change. Sintering of gold nano-inks was studied by Pan *et al.* [12]. An analytical model for neck growth under laser heating was developed and compared with MD simulation result. Although the above-mentioned research efforts, simulation of electric resistivity in low temperature sintering process with the consideration of temperature effect is rarely reported.

In this paper, we develop a molecular dynamics model on sintering of silver nanoparticles at temperature ranges similar to IPL process. Electric resistivity is calculated based on the configuration of silver nanoparticles after sintering. The calculated resistivity is compared against experimental measurement and an analytical solution [15].

2. Modeling details

2.1. Molecular dynamics simulation

To simulate the sintering process at atomistic scale, a molecular dynamics sintering model is developed. Embedded atom method (EAM) [16] is selected to represent the atomic interactions, which has been successfully used for predicting phase transformations, surface energy, and vacancy formation energy in metal and alloy systems. In the embedded atom potential, the energy of atoms is calculated based on atom positions as in the following equation:

$$E_{tot} = \frac{1}{2}\sum_{ij} V_{ij}\left(r_{ij}\right) + \sum_{i} F_i\left(\rho_i\right) \quad (1)$$

where the total energy (E_{tot}) of an atom, I, is represented by pair-wise energy $V_{ij}(r_{ij})$ between atoms i and j, and the atom embedded energy $F_i(\rho_i)$ is described as a function of electron density; r_{ij} is the distance between atoms i and j; ρ_i is the host electron density which is also based on atom positions. Therefore, total energy of the atomistic model is the summation of all atoms in the system. Parameters of this potential function are calculated by density functional theory (DFT) and are fitted according to the structural properties of silver from experiment [17].

Large-scale Atomic/Molecular Massively Parallel Simulator (LAMMPS) [18] code is applied to simulate the sintering process of silver nanoparticles. Atomistic equations of motion based on the potential function are integrated with a time step of 2 fs using velocity-Verlet numeric integrator. Atom trajectories are calculated from each step of integration and used for the next step. To prepare a nanoparticle with realistic atomistic structure, single silver nanoparticle with 6,663 atoms is cut out from a large silver FCC supercell within a radius of 3.0 nm. This spherical particle is then placed in a non-periodic simulation box with shrink-wrapped boundaries to represent an isolated particle. The single particle is equilibrated at constant temperature for 200 ps, with Nose-Hover thermostat canonical (NVT) ensemble. The sintering process of nanoparticle at temperatures of 150 ºC and 200 ºC is studied.

To generate the two-particle sintering model, the single particle is duplicated, and the two particles are placed with an initial center-to-center distance of 6.4 nm. The constructed two-particle sintering model has total 13,362 atoms at 150 ºC, which is shown in Fig. 1. The sintering models are subjected to constant temperatures by rescaling the atom velocity with NVT ensemble for 100 ps. Although in the IPL process, intense pulse light is often applied for duration of 1-10 ms [2],

100 ps is sufficient to capture the initial stage of sintering [19]. The centers of mass and angular momentum for the whole system are subtracted in order to avoid the motion and rotation of rigid body. Atom positions and their velocities are recorded at each 0.1 ps during simulations. Configurational changes are extracted from the atom trajectory. Diameter of each particle is obtained by averaging the upper and lower bounds of the particles. The center of mass for each particle is recorded during simulation, so that the center-to-center distance in the two-particle model can be extracted. A dynamically allocated block region with 0.2 nm thickness is defined between two particles. Neck size is calculated from atoms upper and lower bounds in this region.

The effective conductivity of the two-particle model can be calculated using neck size by Reimann-Weber formula [20]:

$$\lambda_e = \lambda_s \left(\frac{1}{x} + \frac{1}{\pi} \ln \frac{2}{x} \right)^{-1} \tag{2}$$

where λ_e is the effective conductivity, λ_s is the conductivity for bulk silver, and x is the relative neck size normalized by particle radius. The MD calculated neck size and particle size during sintering are used in the equation to calculate the resistivity.

2.2. Analytical model for resistivity predication

The geometric evolution during the initial stage of sintering consists of densification and neck growth. Neck growth is the dominant factor that reduces the resistivity of sintered particles, because it increases the contact cross-sectional area between the particles. Several types of mass transport mechanisms may occur during the sintering process, including viscous flow, plastic flow, evaporation-condensation, and material diffusion [5][21]. All of these different mechanisms may

contribute to the neck growth at the initial stage of sintering [6]. Because mass transport mechanisms compete with each other, it is reasonable to simplify the model to be driven by single transport mechanism [19]. According to Greer [22], for the initial stage of silver sintering at low temperatures, lattice diffusion provides a better fit on experimental data. This is consistent with the results reported by Cheng *et al.* [20, 21], where sintering of nano-sized particles is reasonably explained by crystal structure transformation rather than surface/grain boundary diffusion. Therefore, lattice diffusion is assumed as the major diffusion mechanism in this analytical model for resistivity calculation.

The normalized neck size is calculated by the following equation [19]:

$$\left(\frac{X}{D}\right)^n = \frac{Bt}{D^m} \tag{3}$$

where X is the neck size, and D is the particle size, t is the sintering time, m and n are constants that depend on mass transport mechanism, and B is a factor that also depends on the specific transport mechanism. With the assumption that lattice diffusion is the major driving force for sintering, the factor B can be represented as [19]:

$$B = \frac{80 D_V \gamma \Omega}{RT} \tag{4}$$

where D_v is the lattice diffusion coefficient at temperature T, γ is the surface energy of silver nanoparticle, Ω is the atomic volume (103.5 cm^3/mol), and R is the gas constant. The atomic volume is calculated based on atomic radius of 1.6 Å for silver atom.

In order to determine lattice diffusion coefficient, *Dv*, in equation 4, the mean square displacement (MSD) is calculated using the following equation [23, 24]:

$$MSD = \frac{1}{N}\sum_{i=1}^{N}\left[r_i(t) - r_i(0)\right]^2 \tag{5}$$

$$D_V = \frac{1}{6}\frac{d}{dt}(MSD) \tag{6}$$

where N is the total number of atoms, $r_i(0)$ is the original position of atom i, and $r_i(t)$ is the position of this atom at a given time t. By fitting the slope of the MSDs over time, the diffusion coefficient *Dv* can be obtained from equation 6. The calculated *Dv* is 2.93×10^{-10} m^2/s at 150 °C, and 3.75×10^{-10} m^2/s at 200 °C. Since we only consider lattice diffusion, and equation 5 is suitable for homogeneous system (particle core), the MSDs of the atoms on the surface of the particle (a surface layer of 3 Å thickness) are not computed during simulations. The calculated diffusivities are similar to the MD simulation results of gold nanoparticle by Pan [12], which is higher than the experimentally measured self-diffusivity. The surface energy $\gamma = 1$ J/m^2 is from Medasani's first-principles and empirical computational result [21]. Particle size D is assumed as constant of 6 nm. This is due to the particle size change during the initial state of sintering and is negligible when compared with the neck size change [13].

In the analytical model, the neck growth with respect to the sintering time is calculated based on lattice diffusion mechanism (equation 3), and then the resulting resistivity change over time can be calculated using equation 1.

3. Results and discussion

3.1. Sintering diffusion and neck size evolution

MD simulations of silver two-particle model are performed for 100 ps in isothermal conditions of 150 ºC and 200 ºC, respectively. Configurational changes for sintering at 150 ºC are shown in Fig. 2. The local crystal structures are mapped on each atom according to its coordination number. The particle surfaces are amorphous whereas the interiors remain FCC crystal structure of bulk silver. Since the two particles are initially separated by a distance of 4 Å, at the beginning of sintering, the two particles move towards each other. The initial neck formation starts after 15 ps as shown in Fig. 2(b), and the gap between two particles is filled up. As sintering proceeds as shown in Fig. 2(c), the neck size increases and atoms in the neck region deform to HCP crystal structure starting at 24 ps. This indicates that dislocations in the neck are generated due to the formation of a plane of staking faults between the particles. Final configuration at 100 ps is shown in Fig. 2(d). Neck region grows with additional amorphous atoms filling up the concave region, without the growth of HCP structure region. As explained by Pan [12], the filling up of amorphous atoms may lead to stepwise change of neck size due to the grain boundary sliding effect.

Neck size evolutions during sintering are plotted in Fig. 3. In the beginning of simulation, two particles approach each other due to attraction of neighbor atoms near the neck forming region, and also the long-range interaction of the whole system. Since the initial distances between the two particles are same, the sintering at 200 ºC can begin at earlier time (~ 15 ps) than that at 150 ºC, due to the higher temperature induced atomic mobility. As the sintering continues, neck size increases dramatically during a short time period until point “A” in Fig. 3, followed by a slow neck growth from “A” to “B”. Although the initial stage of sintering is considered from the initial neck formation to point “B”, the neck growth rates change at point “A”. The change in the slope is

mainly due to the strong elastic deformation which increases the neck growth rate before "A"[12]. The sintering after point "B" is considered as the intermediate stage. The intermediate stage of sintering often takes much longer time than the initial stage, with much slower neck growth. Since MD simulations can only capture short time scale phenomenon, usually less than 10 ns, the neck sizes in Fig. 3 almost keep constant afterwards.

In order to understand the atomic diffusion paths during the initial stage of sintering, atomic displacement vectors at 17.6 ps for the sintering temperature if 200 ^{o}C are plotted in Fig. 4. The displacement vectors are calculated based on the position change of each atom during 0.5 ps. It is clear that most atoms in the neck region move either from surface through lattice diffusion, or from grain boundary. This indicates that lattice diffusion is the dominant diffusion mechanism in our MD simulations. This is probably due to that fact that the sintering mechanism at nano-sized particle is mainly due to lattice transformation, which is different from micro-sized powder, as mentioned in Ref. [25]. The result is consistent with the experimental data in previous study [22], and also verifies the assumption of lattice diffusion in our analytical model.

3.2. Resistivity evolution

Substituting the relative neck size from the MD simulated data and assuming $\lambda_s = 1$, the normalized resistivity during the MD of simulated sintering is obtained and compared with analytical model results as shown in Fig. 5. From the MD results at different temperatures, the sintering at 200 ^{o}C shows a lower resistivity when compared with 150 ^{o}C. This is due to the earlier neck formation and the faster neck growth at higher temperature of 200 ^{o}C. As the sintering process

gets close to the intermediate stage, the difference of resistivity at different temperatures becomes smaller, because the rate of neck growth decreases during the sintering process. Resistivities at both temperatures decrease slowly at the intermediate stage of sintering, which is also due to the relatively slow rate of neck growth. The normalized resistivities after 100 ps at both temperatures of 200 ºC and 150 ºC yield to 2.27 and 2.60, respectively.

As shown in Fig. 5, the results of neck growth between the MD and the analytical model (equation 3) show good agreement in the time range of 15~20 ps. Larger deviation is found after 21 ps for the sintering of 150 ºC. This is likely due to the formation of dislocation in the neck region, which involves more complicated diffusion mechanisms that affect the neck growth like plastic flow of dislocations [26]. However, this analytical model fails to predict the resistivity change during the intermediate stage of sintering. Larger discrepancy can be found at time greater than 27 ps. This possibly attributes to two major reasons: (1) lattice diffusion is no longer the dominating diffusion path in the intermediate stage; and (2) due to the highly deformed shape, the structure of two-particle sintering model is not suitable to be represented by the two spherical contact geometry assumption.

Greer [22] measured the electrical resistivity change for silver nanoparticles of 40 nm sintered at constant low temperatures in the range of 100–500 ºC. The MD simulated result in this work is compared with Greer's experimental data. The resistivity with respect to the time is not able to be compared directly, since particle used in the experimental measurement is much larger and the size effect of characteristic sintering time or sintering rate shows non-linear dependency as suggested by Buesser [7]. However, by scaling up the MD simulation time using the relationship $T_{EXP} = 6.667 \times T_{MD} - 103.3$, where T_{EXP} is experimental time in min, and T_{MD} is MD simulation time in ps, one can compare the MD results with the experimental data in the same figure. Fig. *6* plots

the MD simulated results and experimental data with both the MD and experimental time scales. By matching the initial stage of sintering duration from experimental sintering time with the MD simulation, similar trend in resistivity evolution is observed, including the temperature dependency of finalized resistivity and the resistivity reduction curve in the initial stage of sintering.

Resistivity can also be represented as a function of densification, which is another measurable property in experiment for sintering characterization. The densification of MD model can be simply represented by normalized shrinkage using the two-particle model [15]. The normalized shrinkage is defined as $L(t)/L_0$, where L_0 denotes the particle's center-to-center distance at the beginning of sintering, and $L(t)$ is the distance at a given time t. The predicted normalized resistivity with respect to shrinkage is compared against the same experimental measurement in previous study [22], as shown in Fig. 7. It shows that the MD simulation is in excellent agreement with the experimental data. Resistivity at shrinkage near fully dense $L(t)/L_0 = 1$ could not be predicted by the simulation, due to the invalidation of small contact size at high density in atomistic model.

The current work can be further improved by considering defects in the particles, since vacancy can affect the diffusion process. The diffusion coefficient used in this work is calculated from defect-free particles, which allows us can compare the MD results with the analytical expression, equation 3. In general, particles with vacancies should facilitate the sintering process due to added diffusion through vacancies. Additional improvement of this work may include initial particle misalignment effect on neck growth and densification. A similar study of tungsten sintering was conducted using two-particle MD simulation in Ref. [14], in which only slight differences among different misalignment angles were found. In our study, an initial small gap between the two particles is defined (Fig. 2a) to mimic loose powder packing. A rigid rotation to

align the particles is observed before neck formation. Therefore, the particle initial arrangement should not affect the neck growth and densification result very much. Zhang

4. Conclusions

Sintering of silver nanoparticles at low temperatures is studied by molecular dynamics simulations. The major findings are summarized as follows:

1. Resistivity evolutions during the sintering process are calculated using the Reimann-Weber formula with input MD simulation data. The simulation results show that the resistivity decreases rapidly in the initial state of sintering, due to the fast neck formation and neck growth.

2. The predicted temperature-dependent resistivity evolutions are in good agreement with both experimental measurements and analytical model based on lattice diffusion. Higher sintering temperature reduces resistivity due to the increased sintering at neck area.

3. The primary diffusion mechanism in low temperature sintering process is lattice diffusion, as illustrated by atomic displacement vector plot, and also verified by resistivity comparison with experimental measurement.

4. The resistivity evolution from MD simulations shows excellent agreement in experimental measured resistivity versus shrinkage.

Acknowledgement

JZ acknowledges the financial support provided by Walmart Foundation (project title: Optimal Plastic Injection Molding Tooling Design and Production through Advanced Additive Manufacturing).

References

1. Ko, S.H., et al., *Air stable high resolution organic transistors by selective laser sintering of ink-jet printed metal nanoparticles.* Applied Physics Letters, 2007. **90**(14): p. 141103.
2. Kim, H.-S., et al., *Intense pulsed light sintering of copper nanoink for printed electronics.* Applied Physics A, 2009. **97**(4): p. 791-798.
3. Chung, J., et al., *Damage-free low temperature pulsed laser printing of gold nanoinks on polymers.* Journal of heat transfer, 2005. **127**(7): p. 724-732.
4. Buffat, P., *Size effect on the melting temperature of gold particles.* Physical Review A, 1976. **13**(6): p. 2287-2298.
5. Kang, J.S., et al., *Inkjet printed electronics using copper nanoparticle ink.* Journal of Materials Science: Materials in Electronics, 2010. **21**(11): p. 1213-1220.
6. Volkman, S.K., et al., *Mechanistic studies on sintering of silver nanoparticles.* Chemistry of Materials, 2011. **23**(20): p. 4634-4640.
7. Buesser, B., A.J. Gröhn, and S.E. Pratsinis, *Sintering Rate and Mechanism of TiO2 Nanoparticles by Molecular Dynamics.* The Journal of Physical Chemistry C, 2011. **115**(22): p. 11030-11035.
8. Kang, S.-J.L., *DENSIFICATION MODELS AND THEORIES*, in *Sintering*. 2005, Butterworth-Heinemann: Oxford. p. 227-260.
9. Pan, J., *Solid-state diffusion under a large driving force and the sintering of nanosized particles.* Philosophical Magazine Letters, 2004. **84**(5): p. 303-310.
10. Dong, L., et al., *Three-dimensional transient finite element analysis of the selective laser sintering process.* Journal of Materials Processing Technology, 2009. **209**(2): p. 700-706.
11. Mori, K., H. Matsubara, and N. Noguchi, *Micro–macro simulation of sintering process by coupling Monte Carlo and finite element methods.* International Journal of Mechanical Sciences, 2004. **46**(6): p. 841-854.
12. Pan, H., S.H. Ko, and C.P. Grigoropoulos, *The Solid-State Neck Growth Mechanisms in Low Energy Laser Sintering of Gold Nanoparticles: A Molecular Dynamics Simulation Study.* Journal of Heat Transfer, 2008. **130**(9): p. 092404-092404.
13. Zhu, H., *Sintering processes of two nanoparticles: a study by molecular dynamics simulations.* Philosophical Magazine Letters, 1996. **73**(1): p. 27-33.
14. Moitra, A., et al., *Investigation on sintering mechanism of nanoscale tungsten powder based on atomistic simulation.* Acta Materialia, 2010. **58**(11): p. 3939-3951.
15. Frenkel, J., *Viscous flow of crystalline bodies under the action of surface tension.* Journal of Physics, 1945. **9**(5): p. 385-391.
16. Daw, M.S., S.M. Foiles, and M.I. Baskes, *The embedded-atom method: a review of theory and applications.* Materials Science Reports, 1993. **9**(7): p. 251-310.
17. Williams, P.L., Y. Mishin, and J.C. Hamilton, *An embedded-atom potential for the Cu–Ag system.* Modelling and Simulation in Materials Science and Engineering, 2006. **14**(5): p. 817.
18. Plimpton, S., *Fast Parallel Algorithms for Short-Range Molecular Dynamics.* Journal of Computational Physics, 1995. **117**(1): p. 1-19.
19. German, R.M., *Chapter Seven - Thermodynamic and Kinetic Treatments*, in *Sintering: from Empirical Observations to Scientific Principles*. 2014, Butterworth-Heinemann: Boston. p. 183-226.

20. Gusarov, A.V. and E.P. Kovalev, *Model of thermal conductivity in powder beds.* Physical Review B, 2009. **80**(2): p. 024202.
21. Rahaman, M.N., *Ceramic Processing and Sintering*. 2003: Taylor & Francis.
22. Greer, J.R. and R.A. Street, *Thermal cure effects on electrical performance of nanoparticle silver inks.* Acta Materialia, 2007. **55**(18): p. 6345-6349.
23. Zhang, Y., et al., *Molecular Dynamics Study of the Strength of Laser Sintered Iron Nanoparticles.* Procedia Manufacturing, 2015. **1**: p. 296-307.
24. Zhang, Y. and J. Zhang, *Sintering phenomena and mechanical strength of nickel based materials in direct metal laser sintering process—a molecular dynamics study.* Journal of Materials Research, 2016. **31**(15): p. 2233-2243.
25. Cheng, B. and A.H.W. Ngan, *The crystal structures of sintered copper nanoparticles: A molecular dynamics study.* International Journal of Plasticity, 2013. **47**: p. 65-79.
26. Brett, J. and L. Seigle, *The role of diffusion versus plastic flow in the sintering of model compacts.* Acta Metallurgica, 1966. **14**(5): p. 575-582.

List of Figures

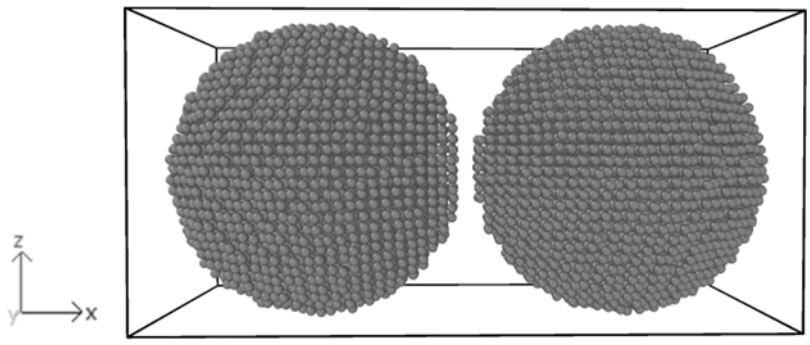

Fig. 1.

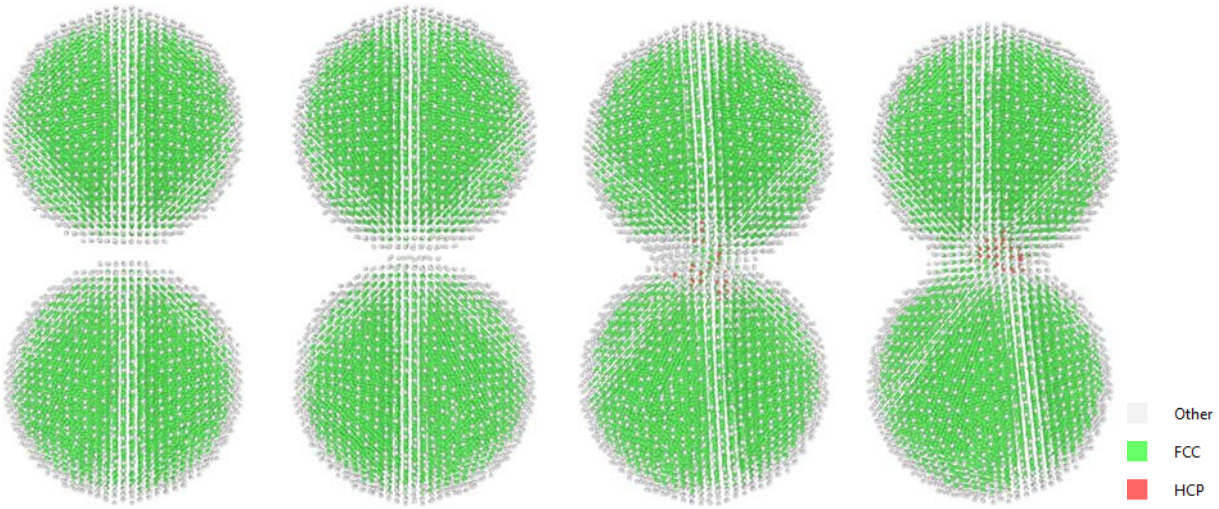

(a) (b) (c) (d)

Fig. 2.

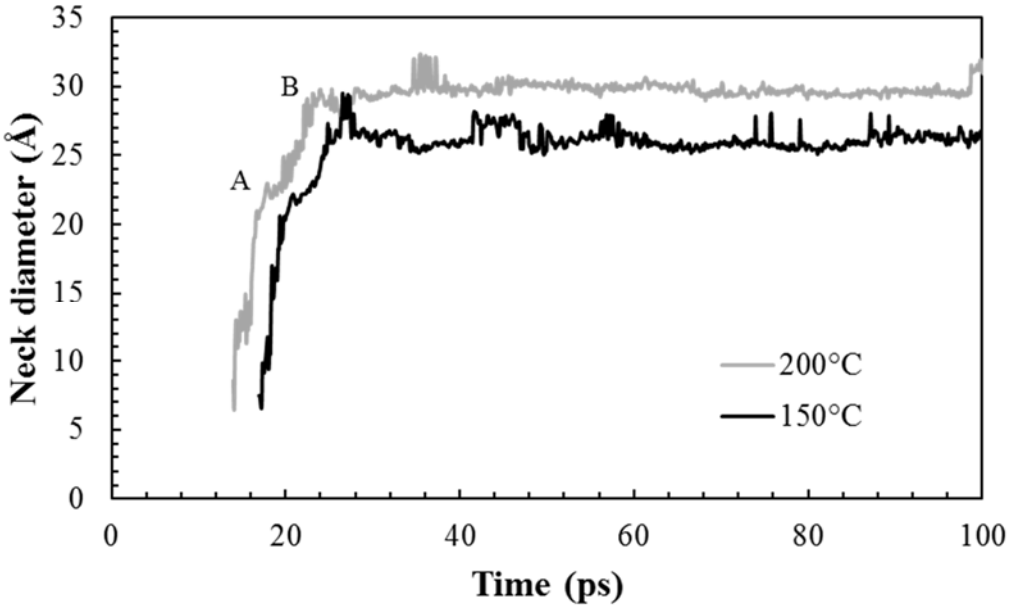
Neck diameter (Å)
Time (ps)
A
B
200°C
150°C
0
5
10
15
20
25
30
35
0
20
40
60
80
100

Fig. 3.

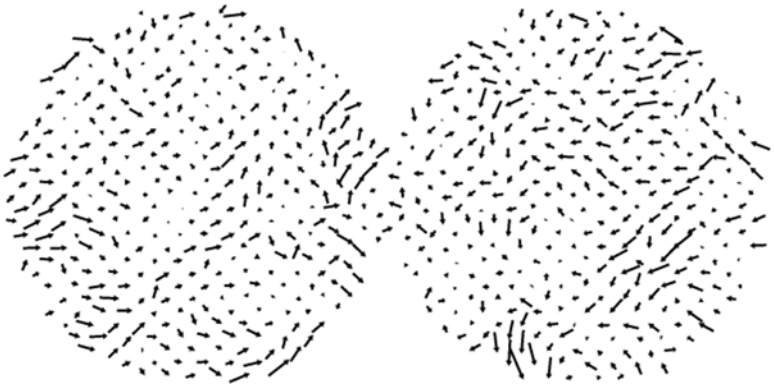

Fig. 4.

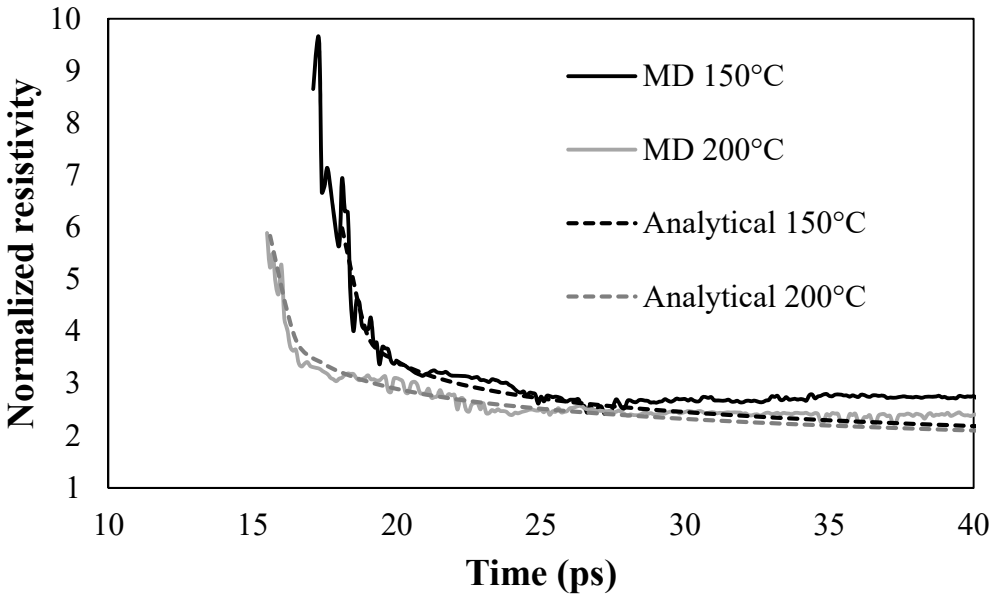
Normalized resistivity
Time (ps)
MD 150°C
MD 200°C
Analytical 150°C
Analytical 200°C
10
9
8
7
6
5
4
3
2
1
10
15
20
25
30
35
40

Fig. 5.

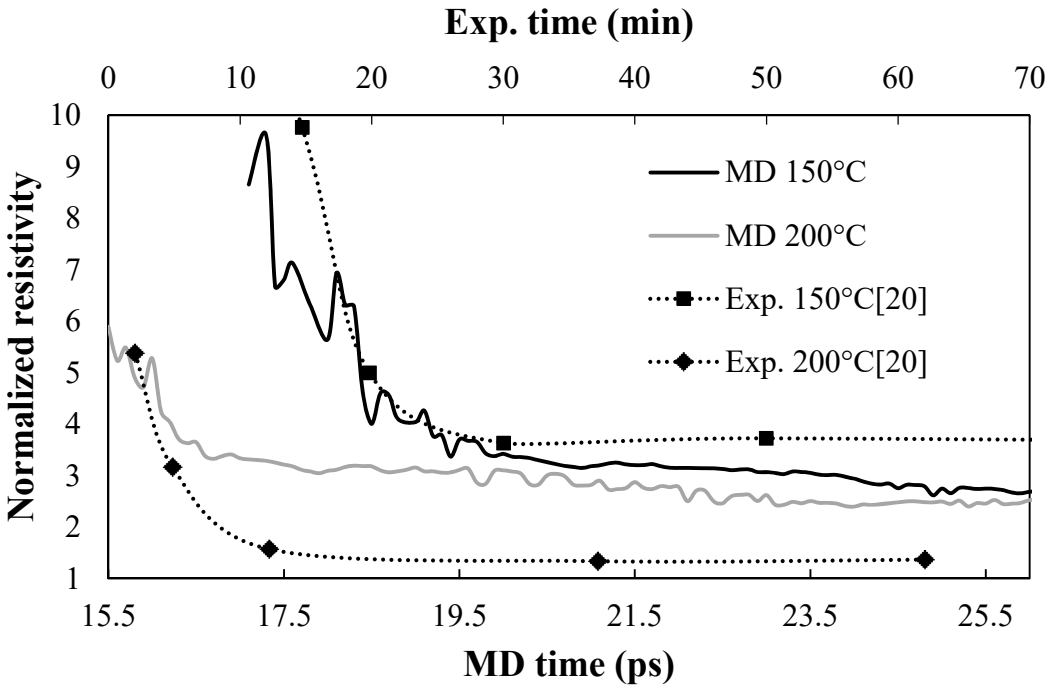
Exp. time (min)
0
10
20
30
40
50
60
70
Normalized resistivity
10
9
8
7
6
5
4
3
2
1
MD 150°C
MD 200°C
Exp. 150°C[20]
Exp. 200°C[20]
15.5
17.5
19.5
21.5
23.5
25.5
MD time (ps)

Fig. 6.

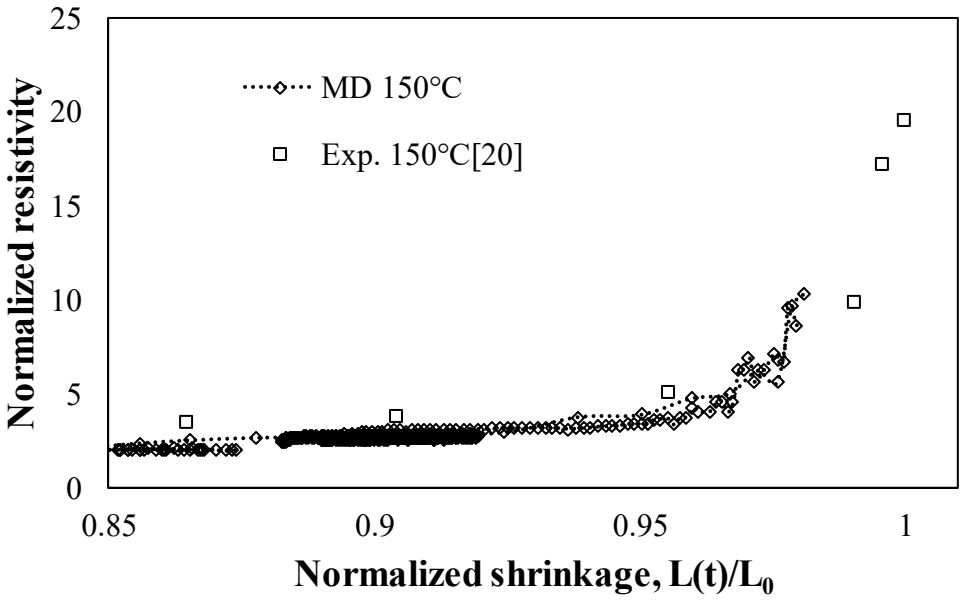
25
20
15
10
5
0
Normalized resistivity
MD 150°C
Exp. 150°C[20]
0.85
0.9
0.95
1
Normalized shrinkage, L(t)/L0

Fig. 7.